INTERNATIONAL JOURNAL FOR NUMERICAL METHODS IN FLUIDS
Int. J. Numer. Meth. Fluids 2002; **38**:1159–1176 (DOI: 10.1002/fld.191)

A numerical study of an unsteady laminar flow in a doubly constricted 3D vessel

B. V. Rathish Kumar[1,3,*], T. Yamaguchi[2], H. Liu[1] and R. Himeno[1]

[1]*Division of High Performance Computing, RIKEN, Wako-shi, Japan*
[2]*Department of Mechanical and Systems Engineering, NIT, Nagoya, Japan*
[3]*Indian Institute of Technology, Kanpur, India*

SUMMARY

Unsteady flow dynamics in doubly constricted 3D vessels have been investigated under pulsatile flow conditions for a full cycle of period T. The coupled non-linear partial differential equations governing the mass and momentum of a viscous incompressible fluid has been numerically analyzed by a time accurate Finite Volume Scheme in an implicit Euler time marching setting. Roe's flux difference splitting of non-linear terms and the pseudo-compressibility technique employed in the current numerical scheme makes it robust both in space and time. Computational experiments are carried out to assess the influence of Reynolds' number and the spacing between two mild constrictions on the pressure drop across the constrictions. The study reveals that the pressure drop across a series of mild constrictions can get physiologically critical and is also found to be sensitive both to the spacing between the constrictions and the oscillatory nature of the inflow profile. The flow separation zone on the downstream constriction is seen to detach from the diverging wall of the constriction leading to vortex shedding with 3D features earlier than that on the wall in the spacing between the two constrictions. Copyright © 2002 John Wiley & Sons, Ltd.

KEY WORDS: unsteady flow dynamics; doubly constricted 3D vessels; pulsatile flow; numerical analysis

INTRODUCTION

Study of unsteady flow dynamics in a multiply constricted 3D vessel has several interesting engineering and medical applications. For instance, tubes with wavy constrictions are used in heat exchangers to enhance heat transfer performance. The reflux condenser is an example of such a system. Patankar *et al.* [1], Sparrow and Prata [2], and Prata and Sparrow [3] etc. have worked with such configurations for analyzing the heat transfer process in a fully developed laminar flow in vessels having streamwise periodic variations of cross-sectional area. Viscous flow past wavy boundaries is of interest to researchers because of its importance in phenomena such as the generation of wind waves on water, the stability of liquid film in

*Correspondence to: B. V. Rathish Kumar, Division of High Performance Computing, Computer and Information Center, RIKEN, 2-1 Hirosawa, Wakoshi, 351-0918 Saitana, Japan.

Received 9 August 2000
Revised 20 February 2001

contact with a gas stream, the transpiration cooling of re-entry vehicles and rocket boosters, film vaporization in combustion, fluid flow in pipes with fittings etc. [4]. It is also of great significance to bio-flow analysts owing to its relationship to localized stenoses, blood and urinary flow, and for the optimal design of artificial organs. Analysis of flow dynamics in a vessel with constriction is of paramount clinical importance in understanding the influence of an arterial stenosis on regional blood flow, i.e. on the perfusion of the distal vascular bed. Further, the possibility of hemodynamic factors participating in the genesis and proliferation of atherosclerosis has fostered increased study on the topic for the last two decades. Numerous investigations on experimental, theoretical and computational fronts have been carried out to trace the pressure–flow relations, hemodynamic factors in a vessel with a single constriction. Studies of Lee and Fung [5], Young and Tsai [6], Daly [7], Deshpande *et al.* [8], Wille [9], O'Brien and Ehrlich [10], Huang *et al.* [11], Rathish Kumar and Naidu [12] etc. are in this direction. These investigations lead to the notion of critical constriction or stenosis, i.e. beyond 75–80 per cent of occlusion any small change in the lumen area produces abrupt changes in the flow through constriction and the pressure distal to it. In some cases the presence of atherosclerotic plaques may lead to the occurrence of secondary stenosis distal to the primary stenosis. In many clinical situations angiograms taken from patients with coronary symptoms have indicated the presence of multiple stenoses in the same artery. Individually, each of these constrictions can be non-critical. However, it is to be investigated whether a number of such noncritical mild stenoses in a series could lead to pressure–flow relations and hemodynamic factor changes similar to a single critical stenosis. Further, if these individual constrictions are spaced sufficiently apart, it seems obvious that each of them can be treated as single constriction. In this non-interacting case their combined effect could be the sum of their individual effects. When these constrictions are positioned close to one another, they would be expected to interact with each other and their combined effect could be different from the non-interacting case. Talukder *et al.* [13] and Van Dreumel and Kuiken [14] have carried out experimental studies related to flow dynamics in doubly contricted vessels. Recently, Lee [15] and Damodaran *et al.* [16] have made 2D steady flow computational analysis of flow in multiply constricted vessels. Especially, the subtle features like vortex formation and shedding demand a full 3D analysis. Now, owing to the energy loss associated with such features the pressure drop across the constrictions associated with 3D flow can be different from what one would get from a 2D analysis.

In this study, 3D unsteady flow dynamics of a viscous incompressible fluid in a non-compliant vessel with two constrictions in a series has been analyzed. A time accurate cell centered Finite Volume Method [17] in conjunction with pseudo-compressibility technique and Roe's flux difference splitting and MUSCL interpolation has been employed in the numerical computations. The effect of Re on pressure drop and velocity distribution as the flow passes through the doubly constricted tube has been analyzed. To understand the interactability of stenoses simulations have been carried out with different spacings between the two stenoses. Further, the subtle features like vortex formation and shedding, stretch of separation zones have also been investigated.

DESCRIPTION OF THE MATHEMATICAL MODEL

Consider a 3D unsteady viscous incompressible Newtonian fluid in a doubly constricted non-compliant vessel in the Cartesian co-ordinate system (x, y, z). The geometry of the vessel is

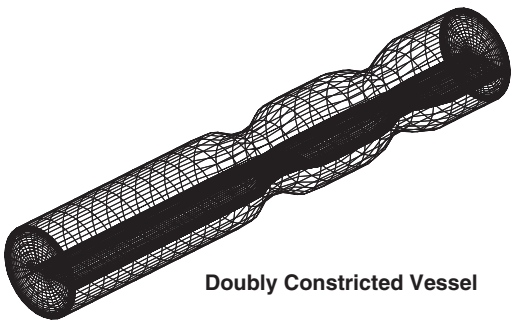

Figure 1. A 3D doubly constricted vessel.

shown in Figure 1. The governing equations are the three-dimensional, incompressible, unsteady Navier–Stokes equations written in strong conservation form for mass and momentum. The artificial compressibility method is used by adding a pseudo time derivative of pressure to the continuity equation. For an arbitrary control volume V, the non-dimensionalized governing equations are:

$$\int_V St\left(\frac{\partial \mathrm{Q}}{\partial t}+\frac{\partial \mathrm{q}}{\partial \tau}\right)\mathrm{d}V+\int_V\left(\frac{\partial \mathrm{F}}{\partial x}+\frac{\partial \mathrm{G}}{\partial y}+\frac{\partial \mathrm{H}}{\partial z}+\frac{\partial \mathrm{F_v}}{\partial x}+\frac{\partial \mathrm{G_v}}{\partial y}+\frac{\partial \mathrm{H_v}}{\partial z}\right)\mathrm{d}V=0 \tag{1}$$

where

$$\mathrm{Q}=\begin{bmatrix}u\\v\\w\\0\end{bmatrix},\quad \mathrm{q}=\begin{bmatrix}u\\v\\w\\p\end{bmatrix},\quad \mathrm{F}=\begin{bmatrix}u^2+p\\uv\\uw\\\beta u\end{bmatrix},\quad \mathrm{G}=\begin{bmatrix}vu\\v^2+p\\vw\\\beta v\end{bmatrix},\quad \mathrm{H}=\begin{bmatrix}wu\\wv\\w^2+p\\\beta w\end{bmatrix}$$

In the preceding equations, β is the pseudo-compressibility coefficient; p is pressure; u, v, and w are velocity components in the Cartesian coordinate system x, y, and z; t denotes physical time, τ is pseudo time, Re is the Reynolds' number, and St is the Strouhal number. Note that the term **q** associated with the

$$\mathrm{F_v}=-\left(\frac{1}{R_e}\right)\begin{bmatrix}2u_x\\u_y+v_x\\u_z+w_x\\0\end{bmatrix},\quad \mathrm{G_v}=-\left(\frac{1}{R_e}\right)\begin{bmatrix}v_x+u_y\\2v_y\\v_z+w_y\\0\end{bmatrix},\quad \mathrm{H_v}=-\left(\frac{1}{R_e}\right)\begin{bmatrix}w_x+u_z\\w_y+v_z\\2w_z\\0\end{bmatrix}$$

pseudo time is designed for an inner-iteration at each physical time step, and will vanish when the divergence of velocity is driven to zero so as to satisfy the equation of continuity.

The boundary conditions are the following:

- at inlet: $u=u(t)=0.5(1-\cos(\frac{2\pi t}{T}+\phi)), v=w=0$
- at outlet: $u_x=v_x=w_x=p=0$
- on solid wall: $u=v=w=0$.

It is to be noted here that pulsatility is brought in by the periodic and oscillatory inflow with the period T. Free flow is assumed at the outlet.

DESCRIPTION OF THE NUMERICAL METHOD

By introducing the generalized Reynolds transport theorem and by employing the Gaussian integration theorem to the first and second integrals in Equation (1), respectively, an integrated form of the governing equations in general curvilinear co-ordinate system is gained as

$$\int_V St\left(\frac{\partial \mathrm{q}}{\partial \tau}\right)\mathrm{d}V + St\,\frac{\partial}{\partial t}\int_V \mathrm{Q}\,\mathrm{d}V + \int_S f\cdot\mathbf{n}\,\mathrm{d}S = 0 \tag{2}$$

where $\mathbf{f} = (\mathbf{F}+\mathbf{F}_v, \mathbf{G}+\mathbf{G}_v,\ \mathbf{H}+\mathbf{H}_v)$; S denotes the surface of the control volume; $\mathbf{n} = (\mathbf{n}_x, \mathbf{n}_y, \mathbf{n}_z)$ are components of the unit outward normal vector corresponding to all the faces of the control volume cell. The relationship between the physical and computational spaces is given as:

$$\begin{cases} \xi = \xi(x,y,z,t) \\ \eta = \eta(x,y,z,t) \\ \zeta = \zeta(x,y,z,t) \\ t^* = t \end{cases} \leftrightarrow \begin{cases} x = x(\xi,\eta,\zeta,t^*) \\ y = y(\xi,\eta,\zeta,t^*) \\ z = z(\xi,\eta,\zeta,t^*)' \\ t = t^* \end{cases} \tag{3}$$

where t^* denotes the time in computational space (ξ,η,ζ). The last term in Equation (2) expresses the net flux across the cell faces. For a structured, boundary-fitted, and cell-centered storage architecture, we can further reform Equation (2) in terms of the semi-discrete form, where (i,j,k) denote the cell index such that

$$St\,\frac{\partial}{\partial t}[V\mathrm{Q}]_{jk} + \mathrm{R}_{ijk} + V_{ijk}\left(St\,\frac{\partial \mathrm{q}}{\partial t}\right)_{ijk} \tag{4}$$

where

$$\begin{aligned} \mathrm{R}_{ijk} = {} & (\hat{\mathrm{F}}+\hat{\mathrm{F}}_\mathrm{v})_{i+1/2,j,k} - (\hat{\mathrm{F}}+\hat{\mathrm{F}}_\mathrm{v})_{i-1/2,j,k} \\ & + (\hat{\mathrm{G}}+\hat{\mathrm{G}}_\mathrm{v})_{i,j+1/2,k} - (\hat{\mathrm{G}}+\hat{\mathrm{G}}_\mathrm{v})_{i,j-1/2,k},\ \text{e.g. } \hat{\mathrm{F}}+\hat{\mathrm{F}}_\mathrm{v} = f\bullet \mathrm{S}_n^\xi \\ & + (\hat{\mathrm{H}}+\hat{\mathrm{H}}_\mathrm{v})_{i,j,k+1/2} - (\hat{\mathrm{H}}+\hat{\mathrm{H}}_\mathrm{v})_{i,j,k-1/2} \end{aligned}$$

$$\mathrm{S}_n^\xi = [S_{nx}^\xi, S_{ny}^\xi, S_{nz}^\xi],\quad \mathrm{n} = [S_{nx}^\xi, S_{ny}^\xi, S_{nz}^\xi]/\mathrm{S},\quad S = \sqrt{{S_{nx}^\xi}^2 + {S_{ny}^\xi}^2 + {S_{nz}^\xi}^2}$$

The term V_{ijk} is the volume of the cell (i,j,k). Note that the unit outward normal vector $\mathbf{n}$ can be calculated using the areas of the cell faces, e.g., s_n^ξ in ξ direction. A detailed description of evaluation of the inviscid flux and the viscous flux can be found in Reference [17].

Implicit algorithm for time-integration

The Pade scheme is employed for the time integration

$$\frac{\partial}{\partial t} = \frac{1}{\Delta t}\frac{\Delta}{1+\theta\Delta}, \quad \text{or} \quad \frac{\Delta(V\mathrm{Q})_{ijk}^{(n+1)} - \Delta(V\mathrm{Q})_{ijk}^{(n)}}{\Delta t} = -\left\{\mathrm{R}_{ijk} + V_{ijk}\left(\frac{\partial \mathrm{q}}{\partial \tau}\right)_{ijk}\right\}^{(n+1)} \tag{5}$$

where parameter θ is taken to be 1 for the implicit Euler scheme with second-order accuracy in time; Δt is the time increment; and $\Delta\mathbf{q} = \mathbf{q}^{(n+1)} - \mathbf{q}^{(n)}$. Thus, Equation (4) can be discretized by replacing the time-related term with Equation (5), such that

$$St\Delta(V\mathrm{Q})_{ijk}^{(n)} + \theta\Delta t\Delta\left[\mathrm{R}_{ijk} + V_{ijk}St\left(\frac{\partial \mathrm{q}}{\partial \tau}\right)_{ijk}\right]^{(n)} = -\Delta t\left[\mathrm{R}_{ijk} + V_{ijk}St\left(\frac{\partial \mathrm{q}}{\partial \tau}\right)_{ijk}\right]^{(n)} \tag{6}$$

The pseudo time-related terms designed for the inner-iteration can be approximated as

$$\begin{aligned}&\theta\Delta t\Delta\left(V_{ijk}St\frac{\partial \mathrm{q}}{\partial \tau}\right)^{(n)} + \Delta t\left(V_{ijk}St\frac{\partial \mathrm{q}}{\partial \tau}\right)^{(n)}\\ &= St\Delta t\left[(1-\theta)\left(V_{ijk}\frac{\partial \mathrm{q}}{\partial \tau}\right)^{(n)} + \theta V_{ijk}\frac{\partial \mathrm{q}^{(n+1)}}{\partial \tau}\right] \approx St\Delta t V_{ijk}\frac{\partial \mathrm{q}^{(n)}}{\partial \tau}\end{aligned}$$

Note that, in the preceding the approximation ($\partial q^{(n)}/\partial\tau = \partial q^{(n+1)}/\partial\tau$) is reasonable because the pseudo time τ is for the inner-iteration and thus is dependent at each physical time step.

Hence, the governing equations become

$$St\frac{\Delta Q_{ijk}^{(n)}}{\Delta t} + \frac{\theta\Delta \mathrm{R}_{ijk}^{(n)}}{V_{ijk}} + St\frac{\partial \mathrm{q}^{(n)}}{\partial \tau} = -\frac{\mathrm{R}_{ijk}^{(n)}}{V_{ijk}} \tag{7}$$

The implicit Euler scheme is also employed (see Equation (5)) for the pseudo time integration. Note that there exists a special relationship between $\mathbf{Q}_{ijk}^{(n)}$ and $\mathbf{q}_{ijk}^{(n)}$ based on Equation (1)

$$\mathbf{Q}_{ijk}^{(n,m)} = \mathbf{I_a}\mathbf{q}_{ijk}^{(n,m)}, \quad \mathbf{\Delta Q}_{ijk}^{(n,m)} = \mathbf{I_a}\mathbf{q}_{ijk}^{(n,m)} - \mathbf{I_a}\mathbf{q}_{ijk}^{(n,0)} \tag{8}$$

where $\mathbf{I_a} = [1,1,1,0]^{\mathrm{T}}$. Superscript m denotes the number of the inner-iteration. With the differencing operator for the pseudo time, the governing equations can be reformed as

$$\begin{aligned}St\left\{\frac{\mathbf{I}}{\Delta\tau} + \theta\frac{\mathrm{I}_a}{\Delta t} + \frac{\theta}{V_{ijk}^{(n)}}\frac{\partial \mathrm{R}_{ijk}^{(n,m)}}{\partial \mathrm{q}}\right\}\Delta q_{ijk}^{(n,m)} &= -\frac{1}{V_{ijk}^{(n)}}[(1-\theta)\mathrm{R}_{ijk}^{(n)} + \theta\mathrm{R}_{ijk}^{(n,m)}]\\ &\quad + \frac{\mathrm{I}_a}{\Delta t}\{(\mathrm{q}_{ijk}^{(n,0)} - \mathrm{q}_{ijk}^{(n,m)})\}\end{aligned} \tag{9}$$

where $\Delta\tau$ is the pseudotime-step size. In order to benefit from both lower memory and computational requirements for the solution of Equation (9), the approximated factorization method of Beam and Warming [18], is used for the LHS and, hence, Equation (9) is

rewritten as:

$$St\left\{\mathrm{I}+\frac{\theta\Delta t\mathrm{I}_t}{V_{ijk}^{(n)}}\frac{\partial \mathrm{R}_{ijk}^{(n,m)}}{\partial \mathrm{q}}\right\}^{(\xi)}\left\{\mathrm{I}+\frac{\theta\Delta t\mathrm{I}_t}{V_{ijk}^{(n)}}\frac{\partial \mathrm{R}_{ijk}^{(n,m)}}{\partial \mathrm{q}}\right\}^{(\eta)}\left\{\mathrm{I}+\frac{\theta\Delta t\mathrm{I}_t}{V_{ijk}^{(n)}}\frac{\partial \mathrm{R}_{ijk}^{(n,m)}}{\partial \mathrm{q}}\right\}^{(\zeta)}\Delta \mathrm{q}_{ijk}^{(n,m)}$$
$$=-\frac{\Delta t\mathrm{I}_t}{V_{ijk}^{(n)}}[(1-\theta)\mathrm{R}_{ijk}^{(n)}+\theta\mathrm{R}_{ijk}^{(n,m)}]+\mathrm{I}_t\mathrm{I}_a\{(\mathrm{q}_{ijk}^{(n,0)}-\mathrm{q}_{ijk}^{(n,m)})\} \tag{10}$$

where $\mathbf{I}_t=\mathbf{I}/(\theta+(\Delta t/\Delta\tau)]$, and $\mathbf{I}$ is a unit matrix. The term associated with the change of volume of the LHS is neglected, which does not affect the accuracy of solution when it converges. Note that taking an infinity pseudo time step Δt reduces the $\mathbf{I}_t$ to a unit matrix. Numerical investigation by Roger *et al.* [19] suggested that this can accelerate the convergence of the inner-iteration. The preceding equations can be further decomposed into three sweeps in the ξ, η, and ζ directions in computational domain. A linear system of equations is finally yielded, in which the discrete form of the matrix from the LHS is tridiagonally banded.

RESULTS AND DISCUSSION

To begin with, code has been validated by simulating the unsteady flow in a straight tube and comparing the results with the standard Womersley's solution as available in the literature [20]. Numerical results are found to be in good qualitative and quantitative agreement with an absolute error of less than 1 per cent. A comparison of the numerical and the analytical solutions is shown in Figure 2. Prior to the code checking, grid validation tests are carried out on four different grid systems i.e. $15\times21\times15$, $21\times21\times15$, $27\times27\times21$ and $31\times31\times21$. It is noticed that with the current numerical scheme as one moves from $21\times21\times15$ grid system to a higher grid systems the qualitative behavior of the results related to the problem remain the same and a quantitative deviation of less than 2% is noticed. This error can further be reduced to less than 0.5% with a slight reduction in the time step size and without any noticeable increase in the number of iterations as the current numerical scheme is in the implicit setting. It is also to be noted that the current unsteady flow investigation is related to a periodic flow and one has to repeat the simulation for each setting till a periodicity is observed, which in this case happens to be three cycles. Each cycle consists of about 1000 time steps and each time step consists of about 5–15 inner iterations pertaining to pseudo time (τ). With $21\times21\times15$ grid system on a PIII machine with a 700 MHz processor it takes about 2.8476 s of CPU time to carry out the calculations of one such inner iteration. On average it takes about 7.91 h for one full cycle to be completed which is almost doubled if we moves onto a $31\times31\times21$ grid system yielding only a marginal gain in the accuracy. The memory requirements (assessed based on data structure in the code) as one moves from a $21\times21\times15$ grid system to a $31\times31\times21$ grid system is enhanced by a factor of 4.3. In view of the enormous amount of computational effort, a $21\times21\times15$ grid system is chosen for flow simulations owing to the gain in computational time and resources and also due to the possible solution behavior as projected by grid validation tests. On the chosen grid system, solution at every time step is obtained to an accuracy of 10^{-6} in the square of the

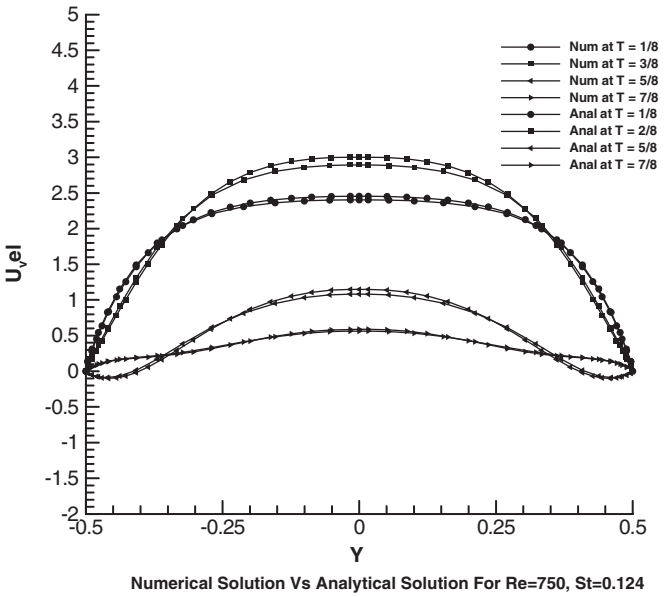

Figure 2. A comparison of the numerical and analytical solutions.

L_2-norm of relative error between two consecutive iterations. Further the results are verified to be solenoidal, i.e. mass conserving.

The parameters that govern the unsteady flow dynamics in a vessel with multiple constrictions are Reynolds' number (Re), Strouhal's number (St), degree of constriction (δ) and the spacing between the constrictions (S). Currently with a focus on time dependent analysis of the influence of interacting stenoses and Re on pressure field and flow field and further on subtle 3D unsteady features like vortex formation and shedding, results pertaining to the numerical simulations with $St = 0.0124$, $\delta = 0.292$ (which leads to 50% constriction), $S = 1, 2, 3, 4, \propto$ (i.e. very large spacing) and $Re = 100, 200, 400, 800, 1200$ have been reported for a full cycle of period (T). The first half of the cycle corresponds to the flow acceleration phase (or systolic phase) and the latter half of the cycle corresponds to the flow deceleration phase (or diastolic phase). Results are reported at $t = [T/i]$, $i = 1, 2, \ldots, 8$.

To begin with, to get an idea of the flow field iso-velocity contours for the settings $Re = 1200$, $S = 1$, $\delta = 0.292$, $St = 0.0124$ for the whole cycle are presented in Plate 1(a)–(h). Owing to the oscillatory nature of the inflow and the geometry of the multiply constricted vessel, interesting contour patterns are seen in the flow domain. In the first part of the systolic phase maximum flow, velocities are seen under the first constriction and in the later half of the systolic phase flow under the second constriction attains maximum velocity. In the diastolic phase the velocities under both constrictions are relatively lower than that found in the downstream region of the vessel. Two concentric circular cellular patterns of iso-velocity regions found at the beginning of the systolic phase under the two constrictions slowly elongate to merge into a single unit by the early diastolic phase and ends up as a complex pattern by the end of diastole. At the end of the systolic phase circular contours of

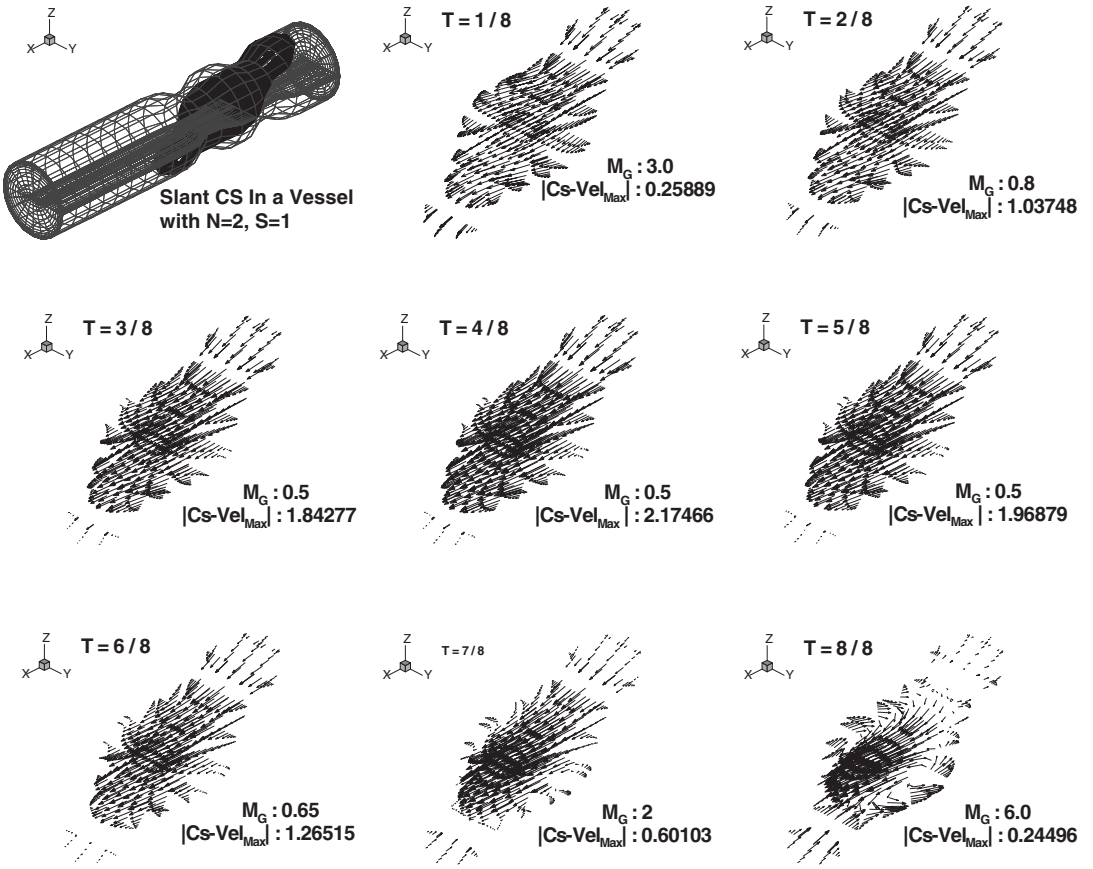

Figure 3. Vector plots on slant CS of the domain for $N = 2,\ S = 1$ at $Re = 1200$. Plots corresponding to $T = I/8,\ I = 1, \ldots, 8$ will be referred to as (a)–(h).

iso-velocity magnitude are seen to manifest near the vessel wall on the downstream side of the constrictions. The circular contours downstream of the second constriction elongates faster and vanishes earlier than those on the wall in the region between the two constrictions. These circular patterns indicate the possible flow separation, stretching and possible vortex formation and shedding. Now, to further investigate the possibility of any such flow separation, vortex formation and for subtle 3D features streamtraces or streamtubes in the form of thin volume lines have been presented in Plate 3(a)–(h). Streamtracing is based on the j-sections Plots in Figure 5 are drawn on the j-section with $j = 5, 15$. In Plate 3(c), corresponding to the beginning of the second half of the systolic phase flow, separation zones are noticed on the diverging walls of the second constriction and also on the walls between the two constrictions. By the end of the systolic phase (Plate 3(d)) both these separation regions stretch to a larger size. While the separation zone on the diverging wall of the second constriction gets much larger and stretches prominently to the downstream side of the vessel, the separation and re-attachment points of the separation zone on the wall between the two constrictions

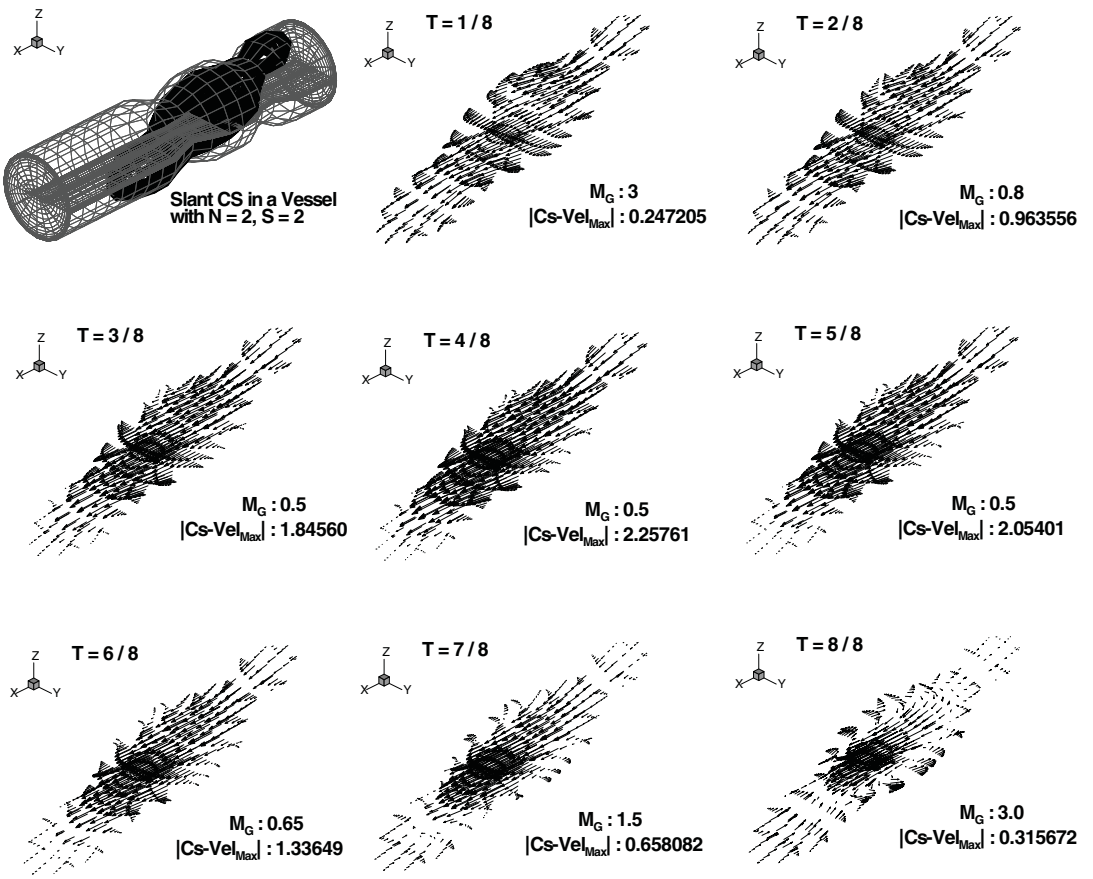

Figure 4. Vector plots on slant CS of the domain for $N=2,\ S=2$ at $Re=1200$. Plots corresponding to $T=I/8,\ I=1,\ldots,8$ will be referred to as (a)–(h).

move further upstream and downstream covering a larger portion of the spacing between the constrictions. As flow gets into the diastolic phase the separation zone on the diverging wall of the second constriction grow faster. From Plate 3(e), one can notice that by $T=5/8$, i.e. the first part of the diastolic phase, the separation zone on the diverging wall of the second constriction has grown larger and is tending towards possible detachment from the wall for vortex shedding. From Plate 3(f), $T=6/8$, it is clear that vortex shedding has already started on the downstream side of the second constriction. During this period, the separation zone on the walls in the spacing between the two constrictions is still growing and getting prominent. From Plate 3(g) corresponding to the first part of the second half of the diastolic phase (i.e. $t=7/8$) the separation zone grows larger covering the hull in the region between the constrictions and is on the verge of detachment from the wall and leading to vortex shedding. By $t=8/8$, i.e. the end of the diastolic phase as seen in Plate 3(f), the vortex shedding has fully taken place. Now from Plate 3(g) and (f) the 3D features of the vortex shedding are

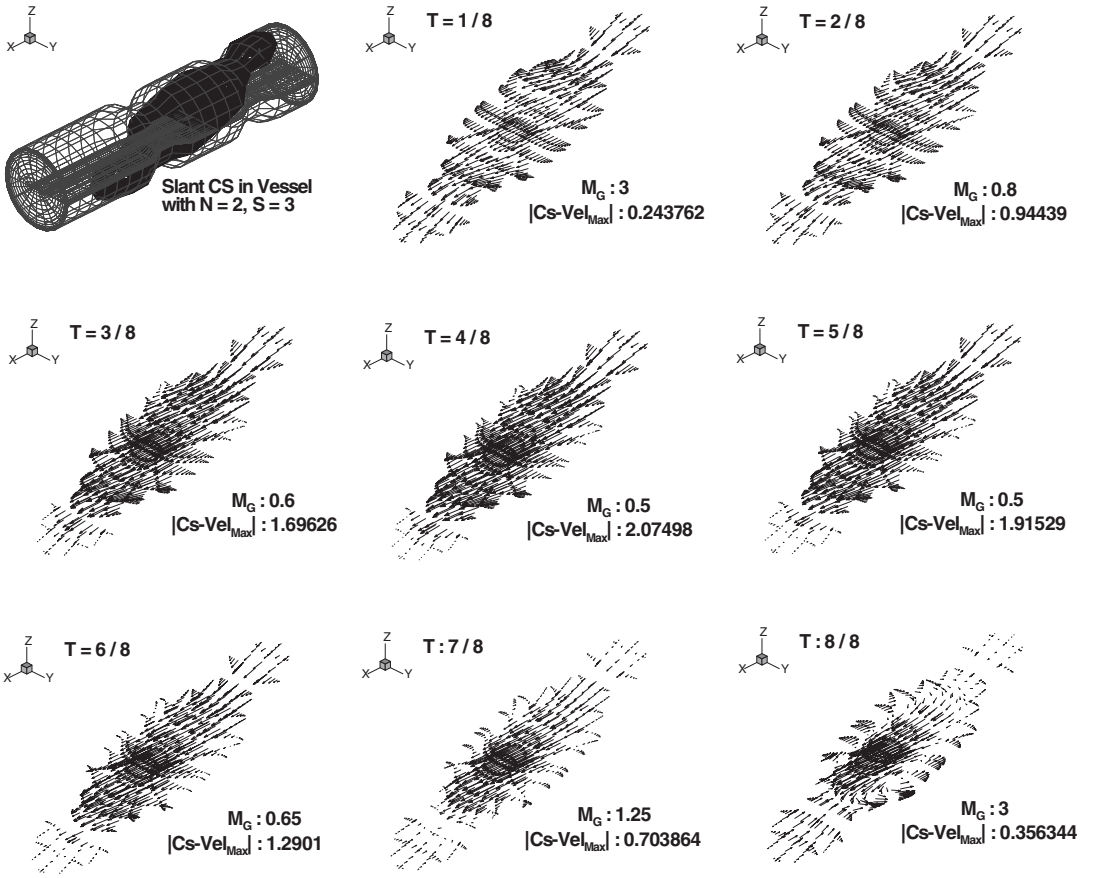

Figure 5. Vector plots on slant CS of the domain for $N = 2,\ S = 3$ at $Re = 1200$. Plots corresponding to $T = I/8,\ I = 1, \ldots, 8$ will be referred to as (a)–(h).

amply clear. It is also to be noted that as shown by the iso-velocity plots by the end of the cycle flow does get complicated and this is fully 3D in nature.

Next, to analyze the influence of the spacing between the constrictions on the observed features, simulations are carried out for the spacings $S = 1, 2, 3, 4, \propto$ (where $\propto$ refers to the case of the vessel with single constriction), $Re = 1200,\ St = 0.0124,\ \delta = 0.292$. Now the results of the study are presented in the form of vector plots on slant cross sections cutting across the constricted regions of the vessel. These results are given in Figures 3–7. In all these figures 'M_G' refers to the magnification of the vector length, '$|\text{Cs-Vel}_{\text{Max}}|$' refers to the magnitude of the maximum velocities found on the slant CS. It may be noted that the plots in Figure 3(a)–(h) correspond to the case presented in Plate 3(a)–(h) and hence can serve as a good reference for understanding Figures 4–7(a)–(h). Figures 3–7(a) depict slant CS on which the vector plots are presented. On closely observing the magnitudes and the direction of the vector lines along the circumference of the slant CS and also the vector lines at the bottom of the CS one can infer the manifestation of the re-circulation zones corresponding

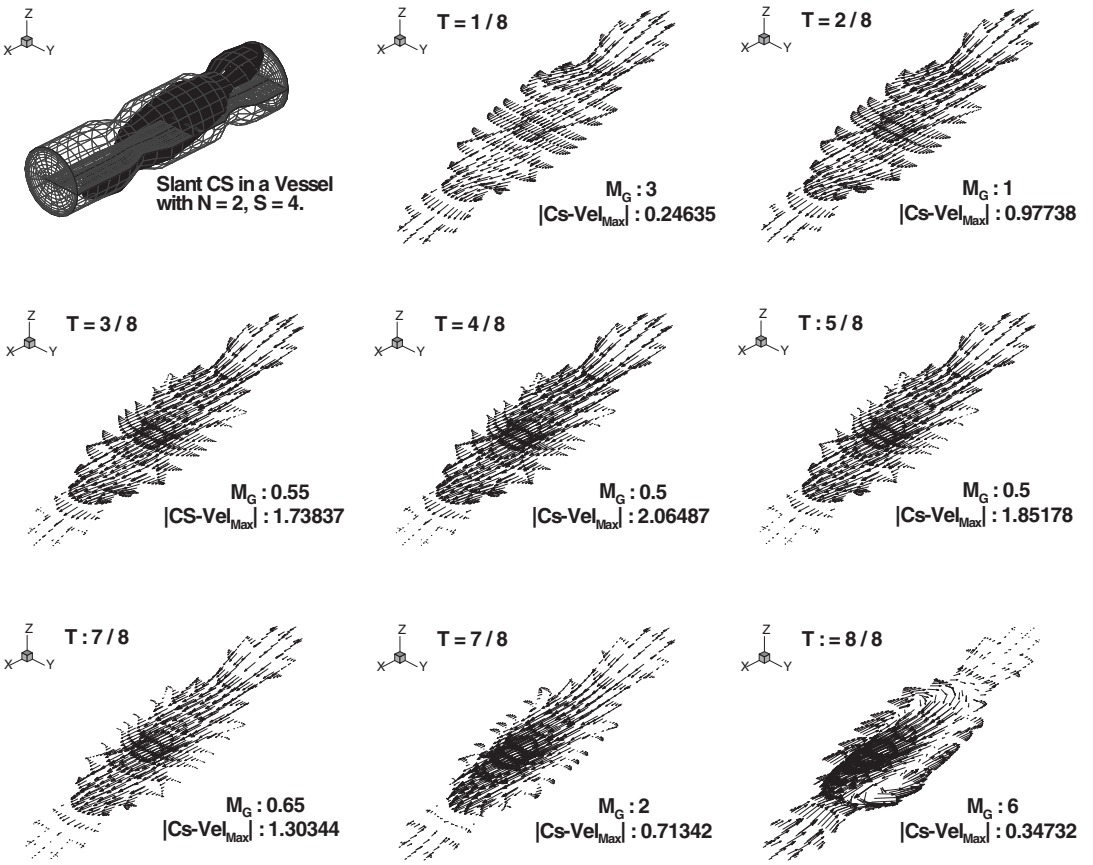

Figure 6. Vector plots on slant CS of the domain for $N = 2,\ S = 4$ at $Re = 1200$. Plots corresponding to $T = I/8,\ I = 1, \ldots, 8$ will be referred to as (a)–(h).

to the zones of flow separation. From Figures 3–6(c) it is clear that the time $t = 3/8$ in all cases flow separation has already manifested both on the diverging walls of the first and the second constrictions. From Figures 3–6(d)–(f) the elongation of these separated zones can be noticed. The vector lines in Figures 3–6(f)–(g) clearly indicate that detachment of the flow separation zone on the diverging wall of the second constriction giving rise to vortices happen in the time interval $(6/8, 7/8)$. The flow separation zones on the walls in the spacing between the two constrictions move away from the wall leading to vortex shedding in the time interval $(7/8, 8/8)$. This is clear from Figures 3–6(g)–(h). Further, as the spacing between the constrictions is increased a re-attachment of the flow separated on the diverging wall of the first constriction does seem to persist till $t = 6/8$, i.e. the first half of the diastolic phase. However, in the second half of the diastolic phase the whole region along the wall in the spacing between constrictions is filled with re-circulation zones. Such a temporal behavior in the flow separation and re-attachment in the spacing between the constriction can affect the pressure drop across the constrictions. Before the pressure field is analyzed, influence of Re on the flow

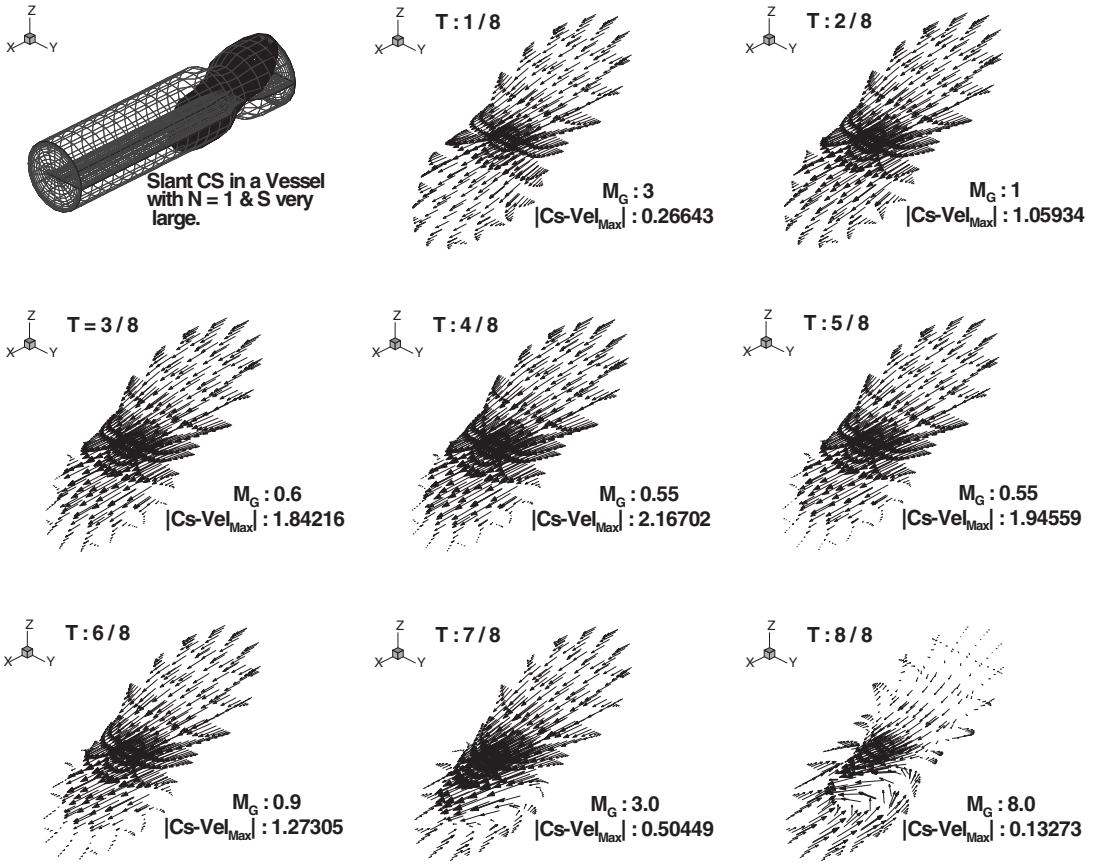

Figure 7. Vector plots on slant CS of the domain for $N = 2,\ S = \infty$ at $Re = 1200$. Plots corresponding to $T = I/8,\ I = 1, \ldots, 8$ will be referred to as (a)–(h).

field is discussed. In Figures 8–10(a)–(h) vector plots for the case $N = 2,\ S = 1, \delta = 0.292$ and $Re = 800, 200, 100$ are presented. Again the features similar to those observed at $Re = 1200$ are clearly noticed at $Re = 800$ and mildly at $Re = 200$. At $Re = 100$ no flow separation is noticed on the diverging walls of both the constrictions and is exactly in agreement with the experimental observations of Talukder *et al.* [13].

To understand the pressure–flow relationship pressure drop across the constrictions has been evaluated. In Figure 11(a)–(h) pressure drop across the constrictions has been plotted against *Re* for various spacing between the constrictions at eight different time steps covering both the systolic and the diastolic phases of a cycle of period ($T = 1$). In all these figures the plot corresponding to the case $S = \propto$ refers to the case with single constriction. During the entire systolic phase and also till the end of the diastolic phase for all the spacing between the constrictions, pressure drops across the two constrictions decrease nonlinearly with the increase of *Re*. Qualitatively this feature is very much in agreement with the results of Talukder *et al.* [13]. During the whole of the systolic phase and in the first half of the diastolic phase there is nearly a two-fold or more increase in the pressure drop for $Re > 200$ as one moves from

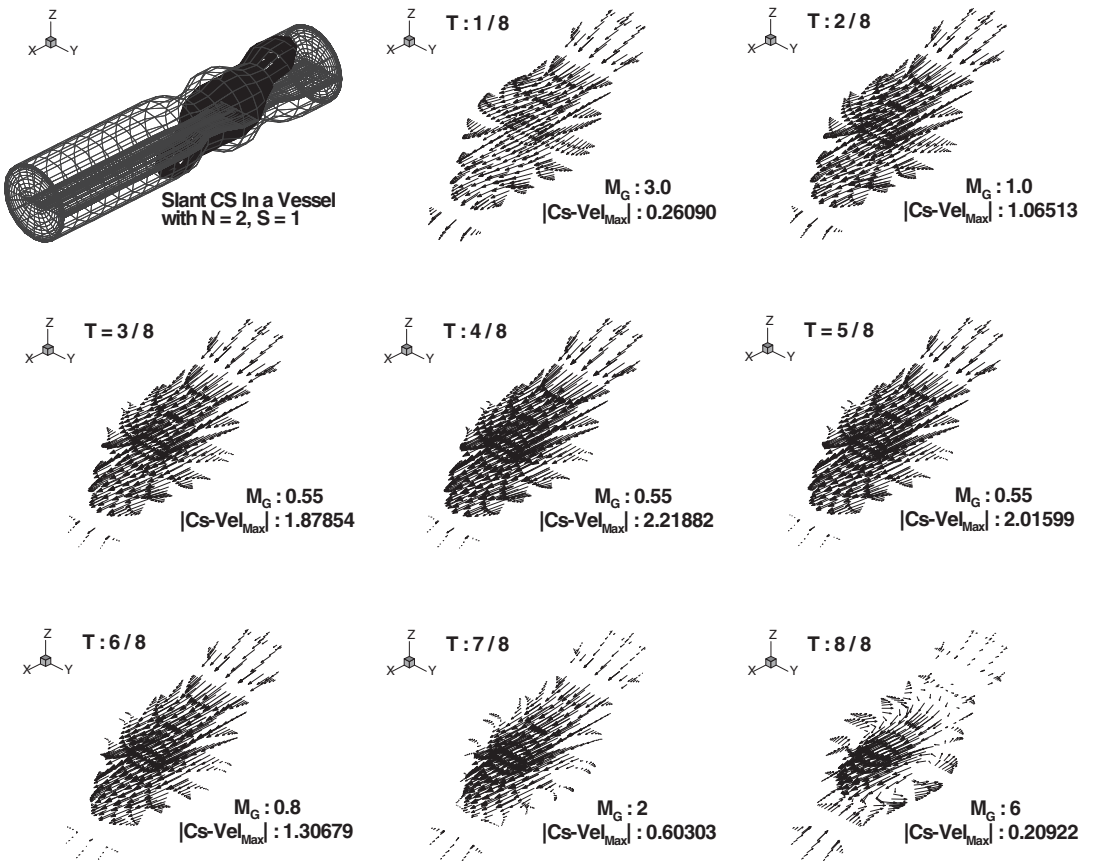

Figure 8. Vector plots on slant CS of the domain for $N = 2,\ S = 1$ at $Re = 800$. Plots corresponding to $T = I/8,\ I = 1, \ldots, 8$ will be referred to as (a)–(h).

a vessel with single constriction to the vessel with double constrictions. This is more vivid with increasing *Re*. This variation in the pressure drop with the increase in the number of constrictions and this degree of sensitivity seem to vary with time, i.e. depends on whether the flow is accelerating or decelerating and also on the exact state of these two phases. In the first half of the systolic phase and also during the second half of the diastolic phase the total pressure drop is found to be larger for smaller spacing between the two constrictions. In the second half of the systolic phase and also during the first half of the diastolic phase the total pressure drop is found to be larger for large spacing between the two stenoses. Recall the discussion on the flow field. It is exactly during the second half of the systolic phase and the first half of the diastolic phase that flow in the case of larger spacing between the constrictions repeatedly undergoes an expansion after each of the two constrictions in series, i.e. the separation zone formed on the first constriction, re-attaches on the wall between the two constrictions. This separation zone subsequently in the latter part of the diastolic phase grows, covering the whole space between the two constrictions and leading to vortex shedding. Energy loss associated with such flow expansion after each constriction will be large and consequently

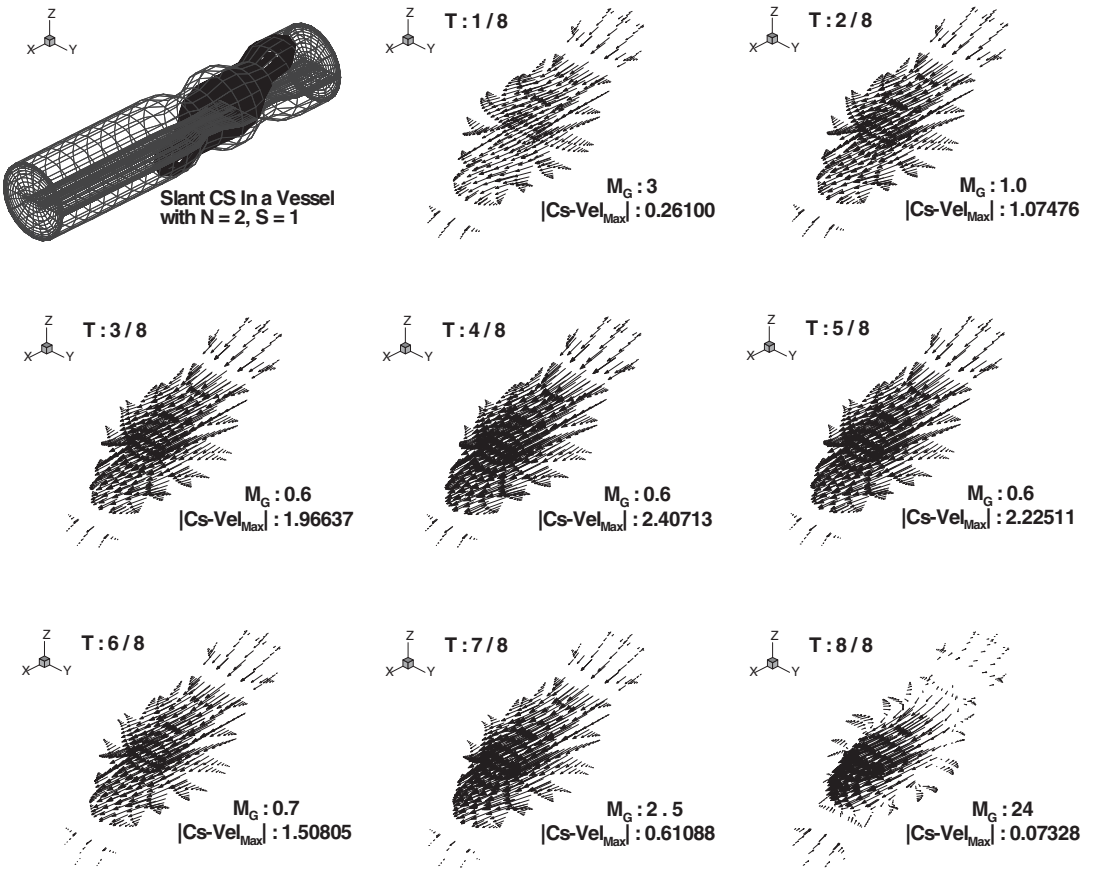

Figure 9. Vector plots on slant CS of the domain for $N=2,\ S=1$ at $Re=200$. Plots corresponding to $T=I/8,\ I=1,\ldots,8$ will be referred to as (a)–(h).

the pressure drop will be higher. The greater pressure drop associated with smaller spacing during the last part of the diastolic phase and early systolic phase may be attributed to the greater energy loss associated with intense re-circulation zones and associated vortex shedding. It is to be noted here that Talukder *et al.* [13] predicted that for $Re \leqslant 100$, increase in the pressure drop with increased spacing is attained within one or two tube diameters. Beyond that point, the pressure drop is relatively independent of spacing. The current study agrees with this prediction except during early systole and during late diastole. However, for $Re > 100$ the current study has shown perceivable variation in pressure drop even for spacing $S=4$ which is at least eight times the diameter of the constricted vessel. It is to be noted here that in the present study vessel walls have been treated to be rigid. Consideration of the compliance in the vessel walls may lead to a small decrease in the above observed factor in pressure drop possibly due to the slight reduction in the intensity of re-circulation flow dynamics.

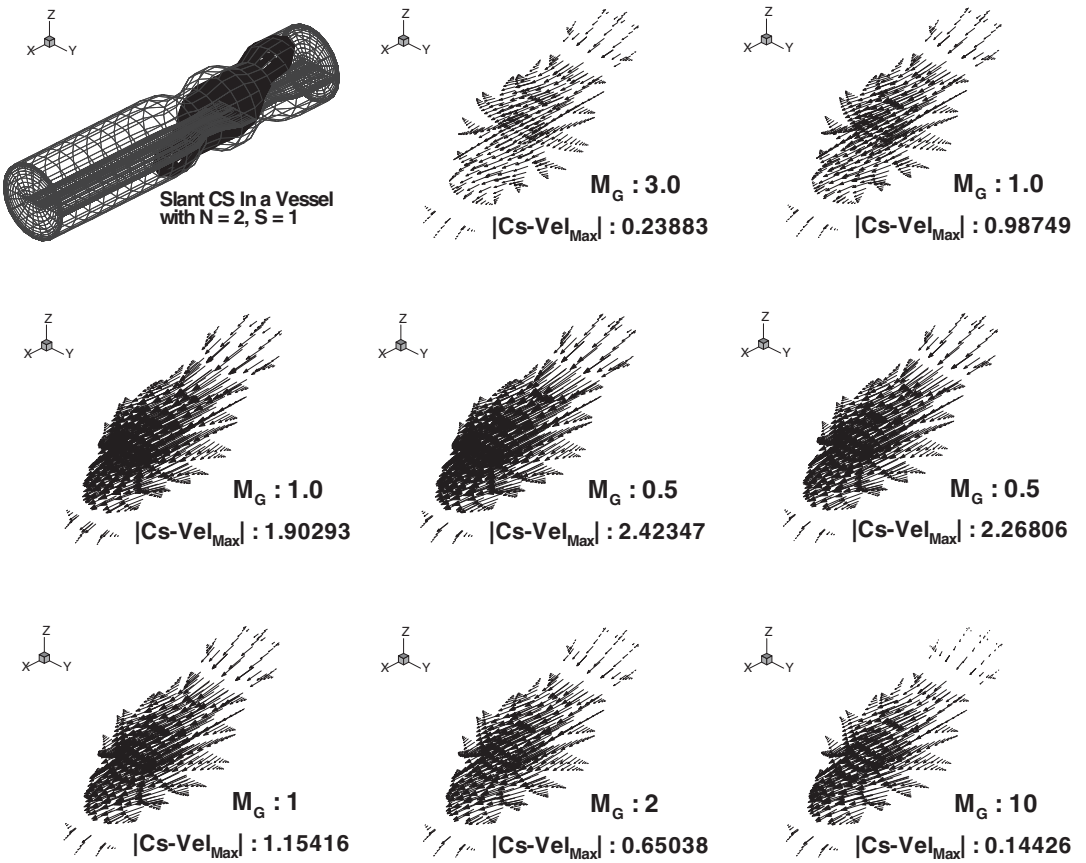

Figure 10. Vector plots on slant CS of the domain for $N = 2,\ S = 1$ at $Re = 100$. Plots corresponding to $T = I/8,\ I = 1, \ldots, 8$ will be referred to as (a)–(h).

CONCLUSIONS

The coupled nonlinear partial differential equations governing the mass and momentum conservations of a 3D unsteady periodic flow in a vessel with two constrictions in a series has been numerically solved employing a time accurate Finite Volume Method. Numerical simulations are carried out for various values of Re, S, fixing St and δ. In comparison with the total pressure drop across a single constriction, the pressure drop across a series of two mild constrictions is found to be significant with the following characteristics:

- Nearly double-fold increase in the pressure drop with the increase in $Re(>200)$.
- In the first half of the flow acceleration phase and also during the second half of the deceleration phase the total pressure drop is found to be larger for small spacing between the two constrictions.

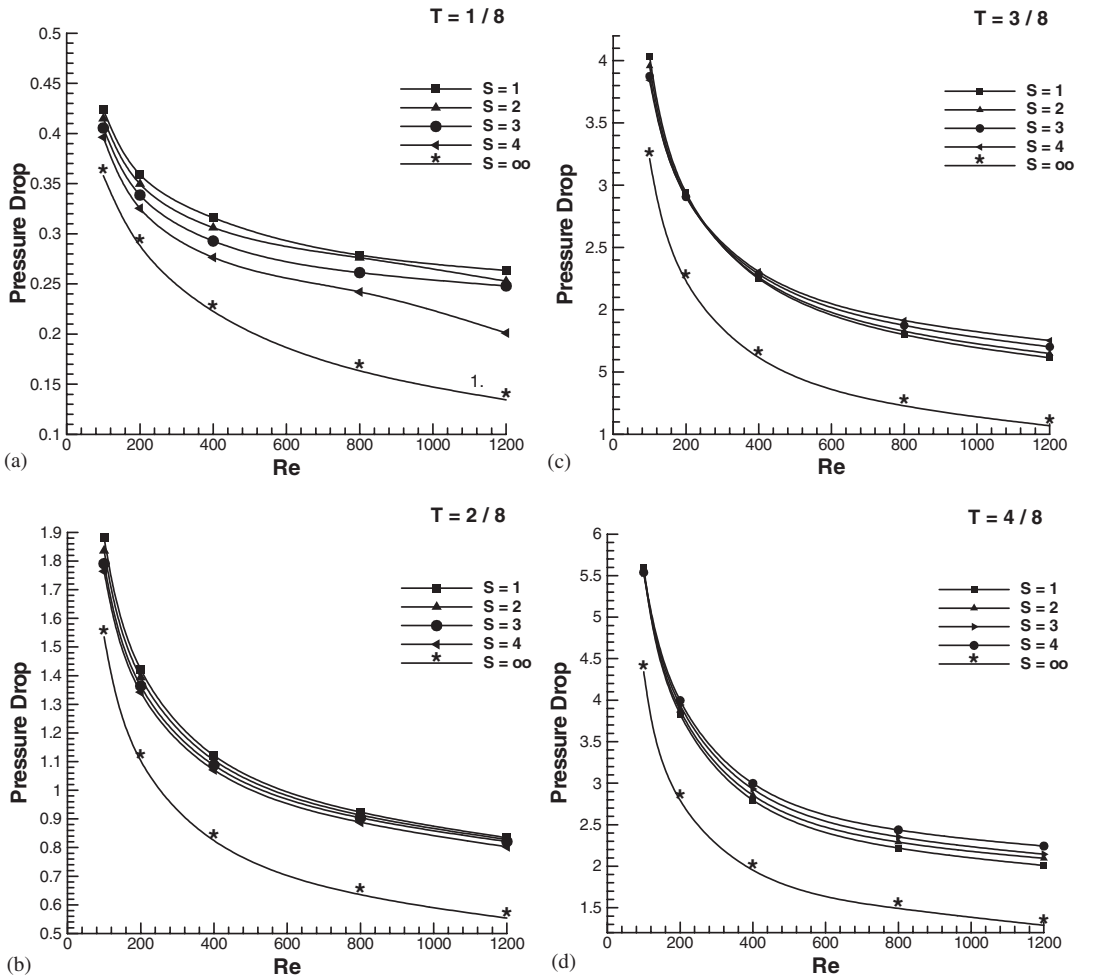

Figure 11. Pressure drop across the two constrictions vs *Re* at different time steps in vessels with varying spacing between the two constrictions in series ($s = \text{oo}$ refers to the case with constriction).

- In the second half of the flow acceleration phase and also during the first half of the flow deceleration phase the total pressure drop is found to be larger for large spacing between the two constrictions.
- Both for single and multiple constriction cases, pressure drop across the constrictions is found to decrease with *Re*.

Flow separation occurs on the diverging walls of both the constrictions. However, the separation zone on the diverging wall of the downstream constriction detaches earlier from the wall than the other separation zone. Prominent vortex shedding with 3D features are seen at the end of the flow deceleration phase in the spacing between the constrictions.

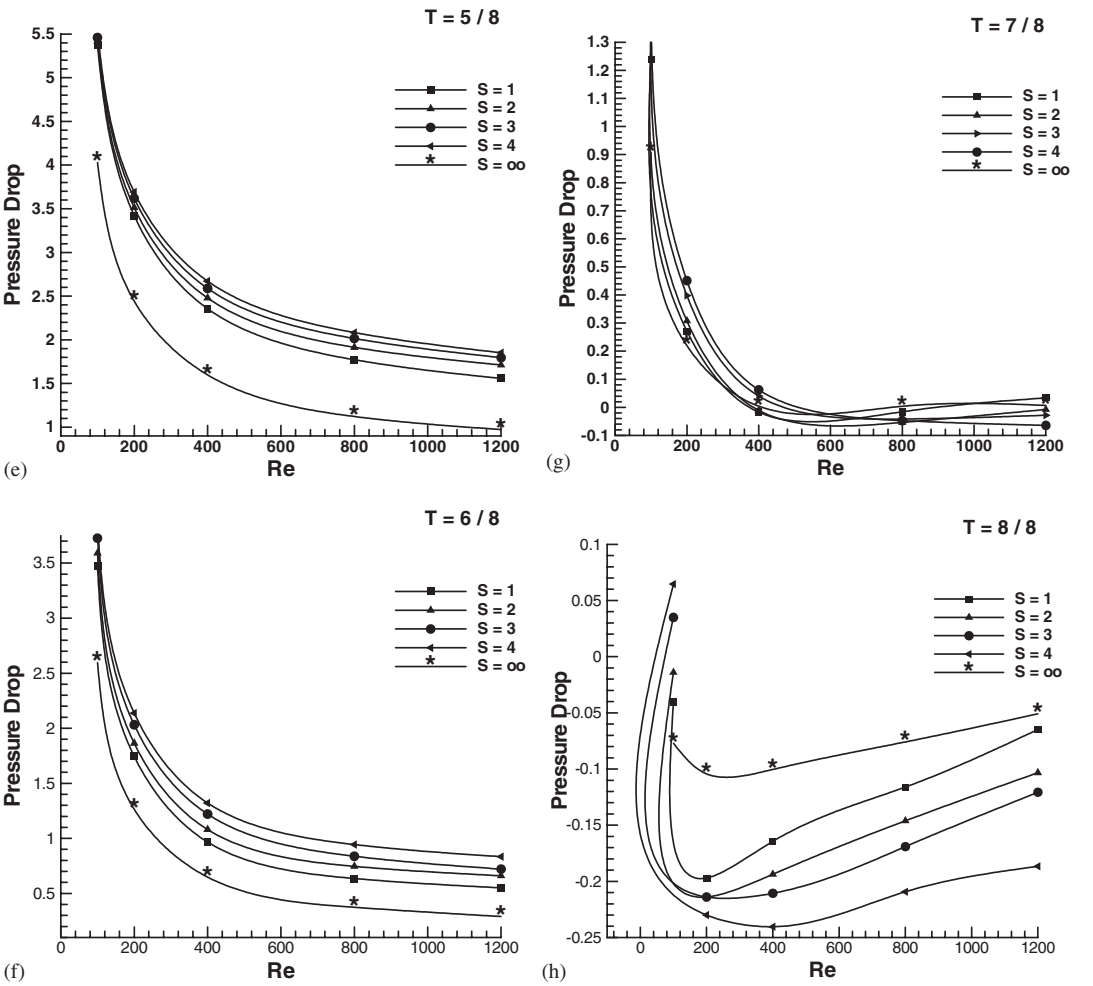

Figure 11. *(continued)*.

The vortex shedding from the re-circulation bubbles leads to the natural question of the presence of any global flow instability. Further, if there is any such global flow instability one has to investigate its relation to the strength of circulation and to the outlet boundary conditions. The authors propose to make a detailed investigation of these issues in the future.

REFERENCES

1. Patankar SV, Liu CH, Sparrow EM. Fully developed flow and heat transfer in ducts having streamwise-periodic variations of cross-sectional area. *ASME Journal of Heat Transfer* 1977; **99**:180–186.
2. Sparrow EM, Prata AT. Numerical solution of laminar flow and heat transfer in periodically converging diverging tube. *Journal of Numerical Heat Transfer* 1983; **6**:441–461.
3. Prata AT, Sparrow EM. Heat transfer and fluid flow characteristics for an annulus of periodically varying cross-section. *Journal of Numerical Heat Transfer* 1984; **7**:285–304.

4. Lee TS. Numerical studies of fluid flow through tubes with double constrictions. *International Journal for Numerical Methods in Fluids* 1990; **11**:1113–1126.
5. Lee JS, Fung YF. Flow in locally constricted tubes at low Reynolds' number. *ASME Journal of Biomechanical Engineering* 1970; **37**:9–16.
6. Young DF, Tsai FY. Flow characteristics in models of arterial stenoses-I: Steady flow. *Journal of Biomechanics* 1973; **6**:395–410.
7. Daly BJ. A numerical study of pulsatile flow through stenosed canine femoral arteries. *Journal of Biomechanics* 1976; **9**:45–475.
8. Deshpande MD, Giddens DP, Mabon RF. Steady laminar flow through modeled vascular stenoses. *Journal of Biomechanics* 1976; **9**:165–174.
9. Wille SO. Pressure and flow in arterial stenoses simulated in mathematical models. *Applied Mathematical Modelling* 1980; **4**:483–488.
10. O'Brien V, Erlich LW. Simple pulsatile flow in a artery with a constriction. *Journal of Biomechanics* 1985; **18**:117–127.
11. Huang H, Modi VJ, Seymour BR. Fluid mechanics of stenosed arteries. *International Journal of Engineering Science* 1995; **33**(6):815–828.
12. Rathish Kumar BV, Naidu KB. A transient UVP finite element analysis of a nonlinear pulsatile flow in a stenosed vessel. *International Journal for Computational Fluid Dynamics* 1997; **9**:71–76.
13. Talukder N, Karayannacos PE, Nerem RM, Vasko JS. An experimental study of the fluid dynamics of multiple noncritical stenoses. *ASME Biomechanical Engineering* 1977: 74–82.
14. Van Dreumel SC, Kuiken GDC. Steady flow through a double converging–diverging tube model for mild coronary stenoses. *Journal of Biomechanical Engineering* 1989; **111**:212–221.
15. Lee TS. Steady laminar fluid flow through variable constrictions in vascular tube. *ASME Journal of Fluids Engineering* 1994; **116**:66–71.
16. Damodaran V, Rankin GW, Zhang C. Numerical study of steady laminar flow through tubes with multiple constrictions using curvilinear co-ordinates. *International Journal for Numerical Methods in Fluids* 1996; **23**:1021–1041.
17. Liu H, Kawachi K. A numerical study of insect flight. *Journal of Computational Physics* 1998; **146**:124–156.
18. Beam RM, Warming RF. Implicit factored scheme for the compressible Navier–Stokes equations. *AIAA Journal* 1978; **15**(4):393.
19. Roger SE, Kwak D, Kiris C. Steady and unsteady solutions of incompressible Navier–Stokes equations. *AIAA Journal* 1991; **29**:1603.
20. Womersley JR. Method for the calculation of velocity rate of flow and viscous drag in arteries when the pressure gradient is known. *Journal of Physiology (London)* 1955; **127**:553–563.

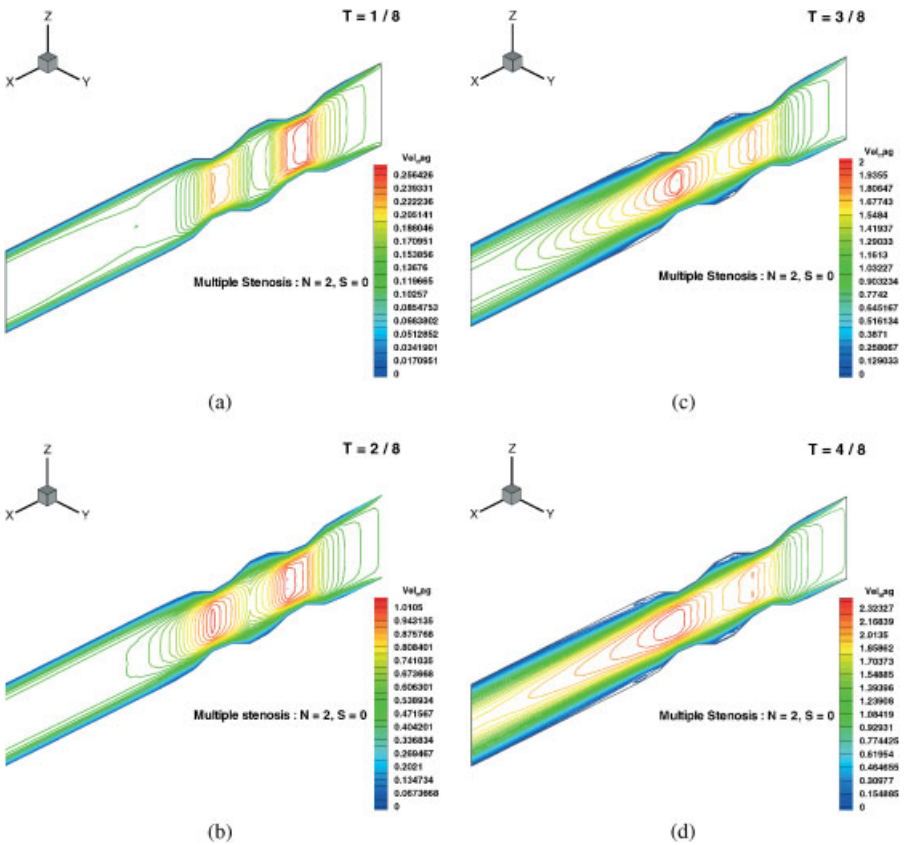

Plate 1. Velocity magnitude contours on a longitudinal CS of the domain at eight different time Steps for $Re = 1200$, $N = 2$, and $S = 1$.

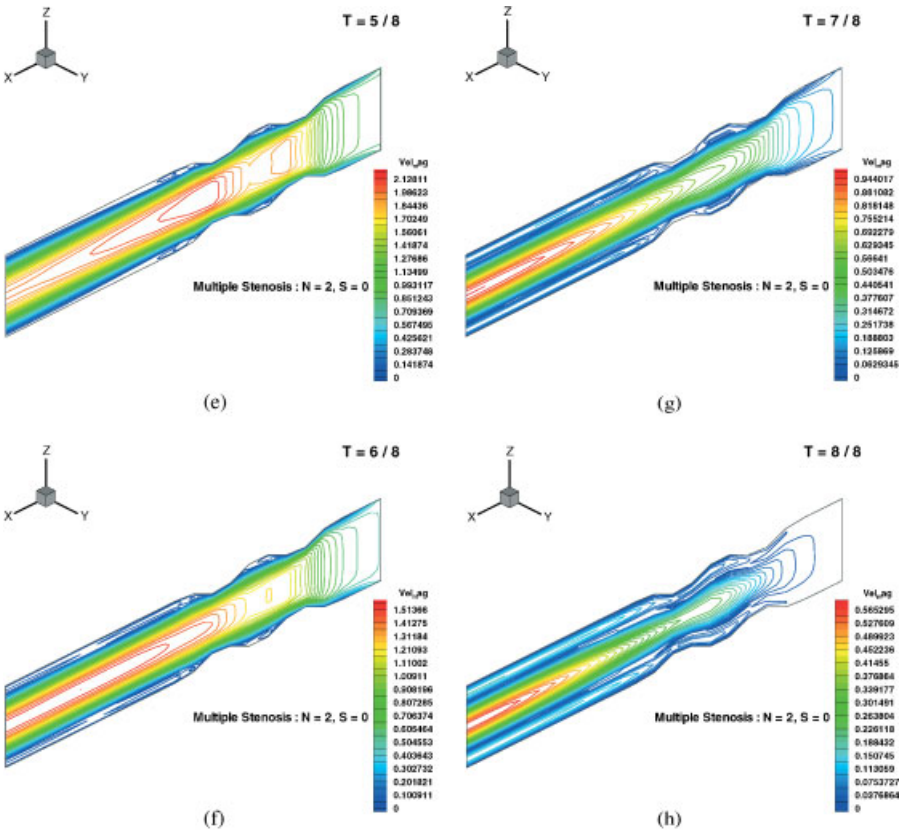

Plate 1. (*continued*).

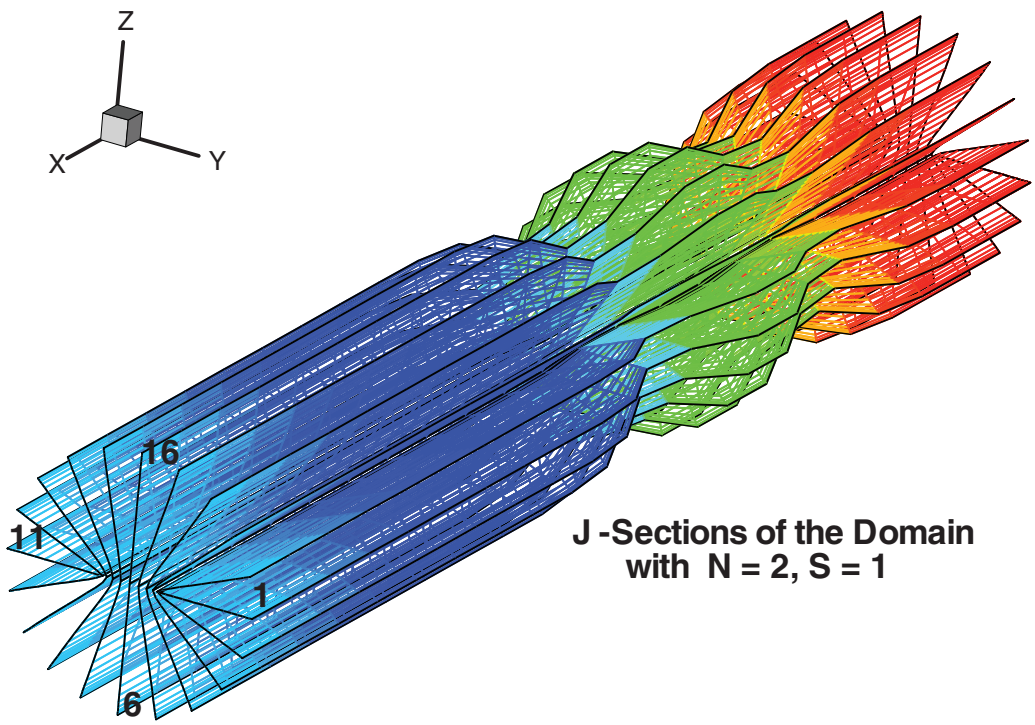

Plate 2. Typical j-sections of the domain.

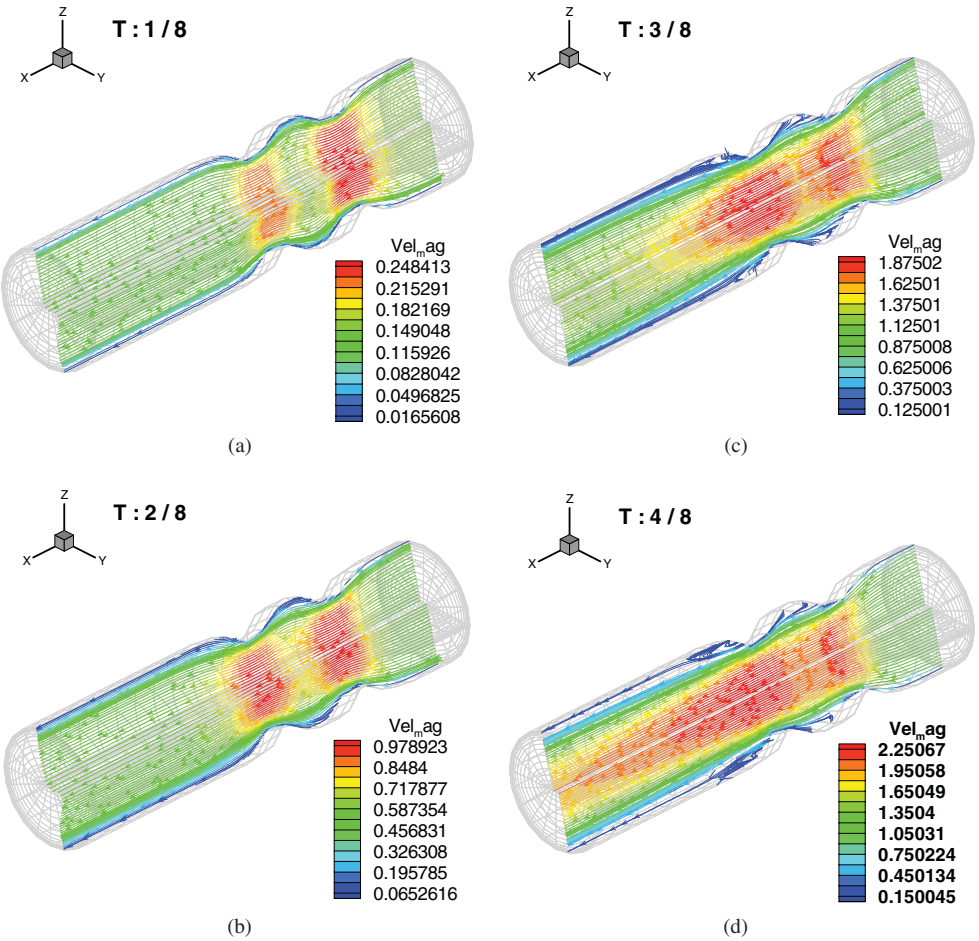

Plate 3. Stream traces on the longitudinal sections $j = 5, 15$ at different time steps for $Re = 1200$, $S = 1$, and $N = 2$.

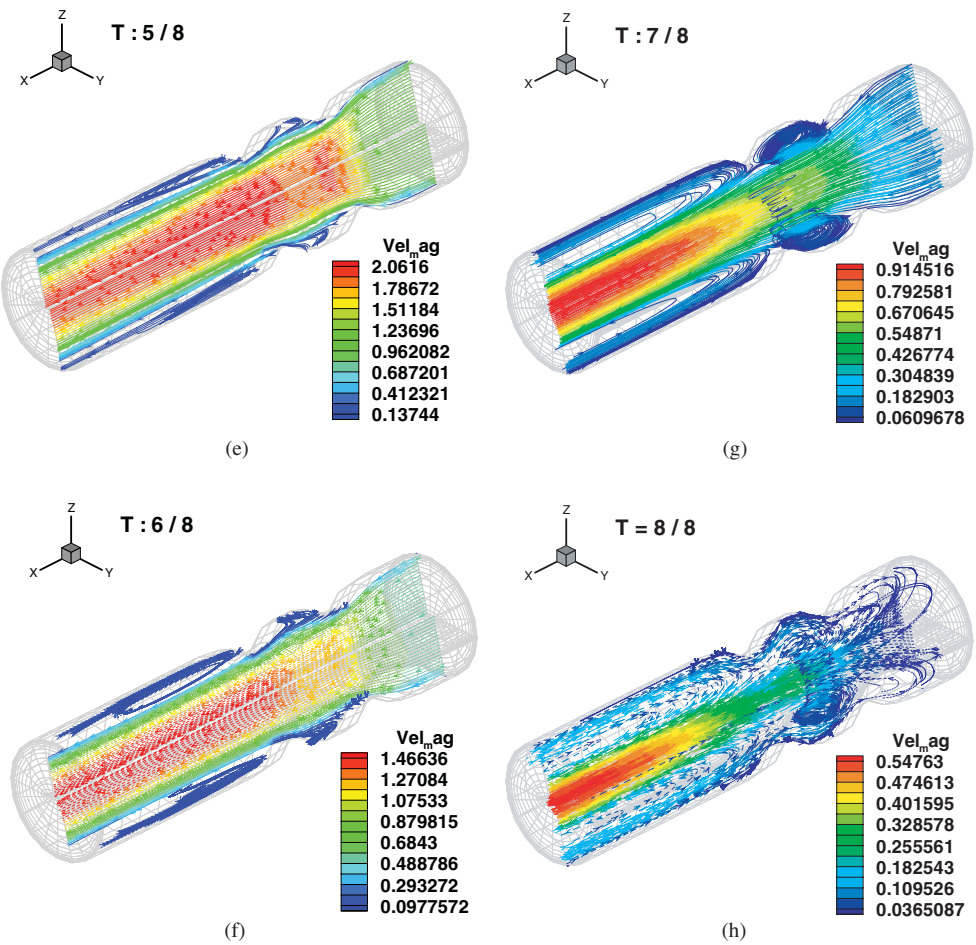

Plate 3. (*continued*).